

X-rays from T Tauri: a test case for accreting T Tauri stars

M. Güdel¹, S. L. Skinner², S. Yu. Mel'nikov³, M. Audard^{4,*}, A. Telleschi¹, and K. R. Briggs¹

¹ Paul Scherrer Institut, Würenlingen and Villigen, 5232 Villigen PSI, Switzerland
e-mail: guedel@astro.phys.ethz.ch

² CASA, 389, University of Colorado, Boulder, CO 80309-0389, USA

³ Ulugh Beg Astronomical Institute, Academy of Sciences of Uzbekistan, Astronomicheskaya ul. 33, Tashkent 700052, Uzbekistan

⁴ Columbia Astrophysics Laboratory, Mail Code 5247, 550 West 120th Street, New York, NY 10027, USA

Received 29 August 2006 / Accepted 8 November 2006

ABSTRACT

Context. The generation of X-rays in accreting T Tauri stars (TTS) is thought to be predominantly due to energy dissipation in magnetic fields, but alternative X-ray generation mechanisms have been proposed, such as heating in accretion shocks near the stellar surface, or in shocks forming in jets.

Aims. We test models and trends discussed in the literature using X-ray data from the classical TTS T Tau.

Methods. High-resolution spectroscopy from the Reflection Grating Spectrometers on XMM-Newton is used to infer electron densities, element abundances and the thermal structure of the X-ray source. We also discuss the ultraviolet light curve obtained by the Optical Monitor, and complementary ground-based photometry. A high-resolution image from Chandra constrains contributions from the two companions of T Tau N.

Results. The X-ray grating spectrum is rich in emission lines, but shows an unusual mixture of features from very hot (≈ 30 MK) and very cool (1–3 MK) plasma, both emitted by similar amounts of emission measure. The cool plasma confirms the picture of a *soft excess* in the form of an enhanced O VII/O VIII Ly α flux ratio, similar to that previously reported for other accreting TTS. Diagnostics from lines formed by this plasma indicate low electron densities ($\lesssim 10^{10}$ cm⁻³). The Ne/Fe abundance ratio is consistent with a trend in pre-main sequence stars in which this ratio depends on spectral type, but not on accretion.

Conclusions. On the basis of line density diagnostics, we conclude that the density of the cool “soft-excess” plasma is orders of magnitude below that predicted for an accretion shock, assuming previously determined accretion rates of $(3\text{--}6) \times 10^{-8} M_{\odot} \text{ yr}^{-1}$. We argue that loading of magnetic field lines with infalling material suppresses the heating process in a part of the corona. We thus suggest that the X-ray production of T Tau is influenced by the accretion process although the X-rays may not form in the bulk of the accretion footprints.

Key words. stars: coronae – stars: formation – stars: pre-main sequence – X-rays: stars – stars: individual: T Tauri

1. Introduction

Low-mass pre-main sequence stars maintain magnetic fields that are thought to provide the energy for high-energy particles and radiation as shown by their strong X-ray and radio emission (for reviews, see, e.g., Feigelson & Montmerle 1999; Feigelson et al. 2007; Güdel 2002, 2004). Vigorous sources of X-ray radiation have been found among class I protostars (e.g., Koyama et al. 1994; Imanishi et al. 2001), accreting classical T Tau stars (CTTS, e.g., Walter & Kuhi 1981; Feigelson & DeCampli 1981), and weak-line T Tau stars (WTTS; e.g., Walter 1986; Neuhäuser et al. 1995) that are no longer surrounded by a thick, accreting disk. A number of observational features have supported a picture in which X-ray emission is due to magnetic coronal processes similar to mechanisms seen in the solar corona: rotational modulation points to a concentration of hot plasma in various magnetic active regions (Flaccomio et al. 2005); flares heat plasma on time scales of minutes to hours,

reaching temperatures of a few tens of MK (Wolk et al. 2005); and electron temperatures continuously exceed 10 MK (e.g., Imanishi et al. 2001; Skinner et al. 2003); such temperatures cannot be achieved by liberating gravitational energy from infall, nor by shocks in moving gas (e.g., jets) commonly observed around young stars at other wavelengths. Also, high-energy electrons observed through their gyrosynchrotron emission give direct evidence for particle acceleration, for which magnetic reconnection processes provide an ideal basis.

Nevertheless, accreting pre-main sequence stars add circumstellar disks and accretion flows to the picture of the stellar environment; stellar magnetic fields may reach out to the inner border of the disk from where they guide lightly ionized mass to the stellar surface (Calvet & Gullbring 1998). WTTS and CTTS are therefore ideal objects to test to what extent the stellar environment controls coronal magnetic fields and energy release. Except for disks and mass accretion streams, the two types of stars appear to be identical in nature, occupying the same region in the Hertzsprung-Russell Diagram (HRD).

Evidence for *some sort* of influence of the disk environment onto X-ray production is broad: i) star-disk magnetic fields may brake stellar rotation, thus damping the magnetic dynamo and

* *New address (since September 2006):* Integral Science Data Centre, Ch. d'Ecogia 16, 1290 Versoix, Switzerland and Geneva Observatory, University of Geneva, Ch. des Maillettes 51, 1290 Sauverny, Switzerland.

inducing weaker overall magnetic activity. In the Taurus Molecular Cloud, for example, CTTS rotate on average less rapidly than WTTS (characteristic rotation periods of $P \approx 8$ d and 2–4 d, respectively; Bouvier et al. 1993). Many TTS may, however, emit at the empirical saturation limit, $L_X/L_{\text{bol}} \approx 10^{-3.5}$, for rotation periods below 10 d (Preibisch et al. 2005), so that a difference between the dynamo operation of CTTS and WTTS may be difficult to identify; ii) despite possible saturation effects, it has now been clearly established that both the X-ray luminosity, L_X , and L_X/L_{bol} are, for otherwise similar stellar characteristics, lower by a factor of ≈ 2 for CTTS than for WTTS (Neuhäuser et al. 1995; Preibisch et al. 2005; Telleschi et al. 2007a). It is unclear in what sense accretion is responsible for this result; iii) on the other hand, the electron temperature of the X-ray emitting plasma may be higher in CTTS than in WTTS (Imanishi et al. 2001; Tsujimoto et al. 2002; Telleschi et al. 2007a); iv) specific changes in the time behavior of X-rays were also observed in outburst phenomena ascribed to strong accretion events in FU Ori-type and EX Lupi-type variables (e.g., a strong flux increase of hard emission during outburst, Kastner et al. 2004a, 2006; or a softening of the X-rays during outburst, Audard et al. 2005).

Recently, a more direct role of accretion has been suggested for the generation of X-rays in CTTS, namely emission from gas that has been shock-heated in the accretion flow near the stellar surface. While free-fall velocities of a few 100 km s^{-1} on CTTS are sufficient to heat shocks to a few MK, a problem is X-ray absorption by the gas stream itself, and by the surrounding photosphere if the shock is buried below the surface (Calvet & Gullbring 1998; Lamzin 1999; Drake 2005). However, the temperatures attained in such shocks are clearly not sufficient to explain the extremely hot X-ray sources of CTTS with temperatures exceeding 10 MK. On the other hand, in the exceptional case of the CTTS TW Hya, X-ray spectroscopic evidence for a predominantly cool plasma led Kastner et al. (2002) to suggest that X-ray production by accretion may be relevant in this star. This conjecture has been further supported by evidence for unusually high electron densities of $n_e > 10^{11} \text{ cm}^{-3}$ derived from density-sensitive line flux ratios of O VII and Ne IX in high-resolution X-ray spectra of the CTTS TW Hya, BP Tau, and V4046 Sgr (Kastner et al. 2002; Stelzer & Schmitt 2004; Schmitt et al. 2005; Robrade & Schmitt 2006; Günther et al. 2006), supported by flux ratios of Fe XVII lines (Ness et al. 2005). Stelzer & Schmitt (2004) further argued that high Ne/Fe and N/Fe abundance ratios may point to accreting gas that is depleted of Fe, presumably because Fe (and several other elements) easily condense onto dust grains further out in the disk, leaving an accreting gas phase enriched by Ne and N.

Two large survey projects of X-ray emission in star-forming regions have addressed the above questions anew. Preibisch et al. (2005) found no support for an accretion scenario in the *Chandra Orion Ultradeep Project* (COUP); the bulk of the observed X-ray emission is related to very hot, coronal plasma. Accretion may in fact suppress the X-ray luminosity by mass loading of magnetic fields. High-resolution X-ray spectroscopy collected in the framework of the *XMM-Newton Extended Survey of the Taurus Molecular Cloud* (XEST) has shown a series of new facets (Telleschi et al. 2007b): i) very high ($\gtrsim 10^{11} \text{ cm}^{-3}$) electron densities are not recorded in all accreting pre-main sequence stars, posing problems for the accretion scenario even in the most favorable case of 100% accretion surface filling; ii) abundance “anomalies”, in particular a high Ne/Fe abundance ratio, are common to many TTS, regardless of whether or not they are accreting. On the other hand, the

Ne/Fe abundance ratio seems to depend on the stellar spectral type; iii) while the bulk plasma observed in CTTS shows very similar thermal properties as plasma in WTTS, there is *soft excess* emission in accreting stars; this excess is visible as (and is defined by) an enhanced ratio of the O VII/O VIII Ly α line fluxes compared with WTTS or zero-age main-sequence (ZAMS) stars. Because the maximum formation temperatures of O VII and O VIII are 2 MK and 3 MK, respectively (and O VIII is formed up to considerably higher temperatures), an enhanced ratio indicates the presence of additional plasma below 3 MK. Observation of this excess requires high-resolution spectroscopy that resolves emission lines formed at 1–4 MK such as lines from O VII or N VI and N VII.

To further our understanding of these issues, detailed case studies are needed. Ideally, a bright source will produce detailed high-resolution grating spectra of the line-dominated range below 1 keV. This allows us to assess anomalies in the thermal structure and electron densities from line ratios. To access lines formed at low (1–4 MK) temperatures (located predominantly at wavelengths longward of 17 \AA), the photoelectric absorption should be moderate (hydrogen column density N_{H} of no more than a few times 10^{21} cm^{-2}). Only few CTTS fulfill these requirements. One of the most outstanding among them is the CTTS T Tau N. We report detailed X-ray spectroscopic and imaging studies of this object, also searching for emission related to its two embedded companions, T Tau Sab.

The specific goal of this paper is to use T Tau as a test case for hypotheses of X-ray production related to magnetic and accretion processes. We add complementary information from optical and ultraviolet observations. The plan of the paper is as follows. In Sect. 2, we introduce the T Tau system, and describe our observations in Sect. 3. Section 4 presents our imaging studies, Sect. 5 introduces light curves, and Sect. 6 presents results from our spectroscopic analysis. Section 7 contains a discussion and our conclusions.

2. Target

Historically, the optically revealed northern component, T Tau N, was the prototype of accreting low-mass pre-main sequence stars. Subsequently, a strongly variable IR companion was found $0'.7$ to its south, now designated as T Tau S. It was soon recognized to be a protostar probably co-eval with T Tau N (Dyck et al. 1982) and dominating the system flux at $\lambda > 2 \mu\text{m}$. The southern component was later found to be double, with a separation of only $0'.09$ or 13 AU (Koresko 2000; Duchêne et al. 2002). An orbital analysis of astrometric radio and infrared data infers masses of $(2.73 \pm 0.31) M_{\odot}$ and $(0.61 \pm 0.17) M_{\odot}$ for Tau Sa and Sb, respectively (Duchêne et al. 2006), suggesting that the former is an embedded Herbig Ae star. The mass of T Tau N is also higher than the masses of typical TTS, namely $M \approx 2.4 M_{\odot}$ (Güdel et al. 2007a), and its rotation period is $P = 2.8$ d (Herbst et al. 1986). The distance to T Tau is ≈ 140 pc (Loinard et al. 2005).

The T Tau triple may be at a critical transition stage between protostars and fully optically revealed TTS; some of its observational properties appear to be related to its particular orientation that places us into an optimal position for observations. van Langevelde et al. (1994a) and van Langevelde et al. (1994b) found evidence for infall of molecular material and a collimated outflow, pointing at 13° to the observer. Solf & Böhm (1999) suggest a pole-on view for T Tau N, which is also clearly supported by mm observations of a well-developed, near-face-on massive accretion disk (Akeson et al. 1998). The latter authors

Table 1. X-ray observing log and coordinates of T Tau.

Parameter	<i>XMM-Newton</i>	<i>Chandra</i>
XEST number	01-045
ObsID	0301500101	3732
Start time (UT)	2005-08-15 13:52:13	2003-10-24 06:11:52
End time (UT)	2005-08-16 12:55:22	2003-10-24 13:37:02
Exposure time	82989 s	26710 s
Coordinates: ^a		
Boresight RA	04 ^h 21 ^m 59.4 ^s	04 ^h 21 ^m 59.69 ^s
Boresight decl.	19 deg 32' 06''	19 deg 32' 20''.6
X-ray: RA	04 ^h 21 ^m 59.44 ^s	04 ^h 21 ^m 59.42 ^s
X-ray: decl.	19 deg 32' 05''.8	19 deg 32' 06''.6
T Tau N: RA ^b	04 ^h 21 ^m 59.43 ^s	04 ^h 21 ^m 59.43 ^s
T Tau N: decl. ^b	19 deg 32' 06''.4	19 deg 32' 06''.4

^a All coordinates are J2000.0. ^b For origin of coordinates, see Smith et al. (2003).

point out that the disk is similar in mass to the solar nebula in which our planetary system formed. The pole-on view of the N component results in a relatively low extinction, while from larger angles all T Tau components would appear to be embedded accreting young stars. A CO emission ring, identified with the outer walls of a bi-conical outflow region, provides evidence that we are looking down into a low-extinction cavity which the stellar wind has nearly swept free of molecular gas (Momose et al. 1996). T Tau Sa appears to be surrounded by an opaque disk seen nearly edge-on (Duchêne et al. 2005, 2006). The disk then is no more than 3 AU in radius given the close orbit of the Sb companion (with a semi-major axis of 11.6 AU and a periastron distance of ≈ 6 AU).

The T Tau system has been detected as a radio source with properties of an extended wind but also of non-thermal radio emission (Phillips et al. 1993; Skinner & Brown 1994), including gyrosynchrotron emission from an outflow (Ray et al. 1997) and strongly polarized emission from magnetic fields inferred to be of kGauss strength (Smith et al. 2003; Loinard et al. 2005). The T Tau system was well detected in X-rays with the *ROSAT* PSPC (Neuhäuser et al. 1995; Stelzer et al. 2000), with a quiescent count rate of (0.03 ± 0.009) cts s⁻¹, and multiple energetic and rapid flares developing on ~ 1 h timescales and reaching up to 0.2 cts s⁻¹.

3. Observations and data reduction

Table 1 summarizes basic parameters of our *XMM-Newton* and *Chandra* X-ray observations, including the centroid coordinates of the X-ray images of T Tau. Both exposures comprise data of four stellar/substellar systems that are thought to be members of the Taurus Molecular Cloud: these are, apart from the T Tau system, the M0 CTTS IRAS 04187+1927, the WTTS RX J0422.1+1934, and the brown dwarf 2M J04221332+1934. All have been detected as X-ray sources. Further details on the former two stars are summarized in Güdel et al. (2007a), while the brown dwarf is described in Grosso et al. (2007).

We obtained an ≈ 83 ks exposure of the T Tau system on August 15–16, 2005, with *XMM-Newton* (Jansen et al. 2001) using standard observing setups¹. Specifically, the European Photon Imaging Cameras (EPIC) obtained images with an angular resolution of ≈ 4 – $5''$ (FWHM), using the full window with a diameter of 30' for the PN camera (Strüder et al. 2001), while

the MOS1 and MOS2 cameras (Turner et al. 2001) observed in the large-window (W3) and small-window (W2) configurations that constrain the central CCD to a field of $5.5' \times 5.5'$ and $1.8' \times 1.8'$, respectively. These constrained window modes were chosen to prevent the detectors from pile-up effects in case of strong flares (but no strong flares that would induce pile-up were actually observed). All EPIC cameras used the medium blocking filter.

The two Reflection Grating Spectrometers (RGS, den Herder et al. 2001) were operating in spectroscopy mode, providing X-ray spectra with a resolution of approximately 60–70 mÅ (FWHM) in the wavelength range of 5–35 Å. Two chip failures earlier in the mission left a gap in the RGS1 spectrum in the range of 10.6–13.8 Å and in the RGS2 spectrum in the range of 20.0–24.1 Å.

The Optical Monitor (OM, Mason et al. 2001) observed in imaging and high-time resolution mode with the UVW1 ultraviolet filter inserted. The latter transmits light roughly in the 2500–3500 Å range. The imaging field of view is a square with a size of $17' \times 17'$. The high-time resolution recording applies, however, only to a central window of $10.5'' \times 10.5''$ in which T Tau was positioned.

The X-ray data analysis of the *XMM-Newton* observations is described in detail by Güdel et al. (2007a). For details on the OM data reduction, see Audard et al. (2007). The data reduction made use of standard SAS v.6.1.0 software (i.e., the epchain, emchain, rgsproc, omfchain, and omichain tasks). Spectra and images were extracted with the evselect task. For the EPIC data, we used canned response matrices appropriate for SAS v.6.1.0, whereas ancillary response files (ARFs) were generated using the SAS task arfgen. The RGS response matrix was generated with the rgsrmfgen task. Background radiation fluctuated between a high and a low level during the observation, each occupying approximately half of the time. The high particle radiation can affect accurate background subtraction in both RGS, in particular in long-wavelength regions where the observed, true continuum is low and suppression of the source spectrum by photoelectric absorption may be severe. We have experimented with either extracting only low-background data, or with constraining the width of the source extraction region in the RGS detector plane. We found that extracting 70% (down from standard 90%) of the PSF width was optimum, and this choice was preferred to selecting in time while keeping the extraction width at the standard value.

The nearby WTTS RX J0422.1+1934 was bright enough (amounting to 41% of the count rate of T Tau in the EPIC detectors, see Güdel et al. 2007a) that it slightly contaminated the background region on the RGS detector. The source region of this star was therefore excluded from the background region of T Tau. It does not directly contaminate the T Tau spectrum, however, as it is located at the edge of the RGS detector, far outside the standard spectral extraction width for T Tau.

We further obtained a *Chandra X-Ray Observatory* (Weisskopf et al. 2002) exposure of 26 ks duration, using the High Resolution Camera (HRC-I, Murray et al. 2000) with a spatial resolution of $\approx 0.5''$ but no energy resolution in the X-ray range. The HRC field of view is about 30' in diameter. The data were reduced using standard CIAO v.3.0.2a software tools². New level 1 events were created with the hrc_process_events task, and level 2 events after applying filters and good time interval (GTI) selection. A light curve analysis revealed no significant variability. A formal source detection was performed with

¹ see *XMM-Newton* User's Handbook (<http://xmm.vilspa.esa.es/>)

² http://cxc.harvard.edu/ciao/guides/hrc_data.html

the wavdetect algorithm in order to obtain precise centroid coordinates for the T Tau source.

We obtained ground-based optical observations of T Tau during three nights around the *Chandra* observations. Photometric monitoring was performed in the *UBVR* bands with the 48-cm AZT-14 reflector at the Mt. Maidanak Observatory during the nights of 2003 October 22/23, 23/24, and 24/25. For these observations we used a single-channel photoelectric photometer in pulse-counting mode, and the photometric data were reduced to Johnson’s international system. We observed HD 27560 as a comparison star and HD 284415 as check star. Other observational information can be found in Mel’nikov et al. (2005).

4. A high-resolution X-ray image of T Tau

The T Tau triple with a separation of $0''.7$ between the N and S components cannot be resolved by the *XMM-Newton* EPIC cameras. The *Chandra* HRC image, on the other hand, could marginally reveal binary structure if the N and S components showed comparable flux levels. The centroid coordinate of the stellar X-ray image (Table 1) is very close to T Tau N.

Figure 1 shows the HRC-I image of the T Tau source. We modeled a point-spread function (PSF) using the CIAO task *mkpsf*. For this, we used a circle with a radius of 15 pixels (with a pixel size of $0.13''$) around the centroid. The PSF was then fitted to T Tau image in the *Chandra* *sherpa* software (Freeman et al. 2001) (the version implemented in CIAO version 3.3.0.1 was used). The model also contained a spatially constant background. We found the centroid to be slightly but insignificantly offset from the true stellar position (offset “X-ray minus true” of $-0''.11$ in RA and $0''.25$ in declination³).

Next, two PSFs were fitted, now assuming two sources with fixed (offset-corrected) positions, the correct relative coordinates, and the same PSF width. Although a very faint extension toward the S is suggested in the *Chandra* X-ray image, the best-fit amplitude at this position is only $(6.5 \pm 2.7)\%$ of the amplitude of the T Tau N model, and is therefore at best a marginal detection (at the 2.4σ level).

In summary, the *Chandra* HRC image (Fig. 1) shows that T Tau N is the principal contributor to the X-ray source. This finding is supported by spectral analysis below that shows low photoelectric absorption compatible only with T Tau N. A small contribution from T Tau S cannot, however, be excluded. Because its visual extinction is $A_V > 8$ mag (for T Tau Sb, Duchêne et al. 2002), we expect a hydrogen column density of $N_H > 1.6 \times 10^{22} \text{ cm}^{-2}$, assuming standard gas-to-dust ratios (Vuong et al. 2003). Some counts could therefore be expected at energies above $\approx 1.5\text{--}2$ keV only. We estimated an X-ray luminosity of T Tau S with the PIMMS software⁴, adopting $N_H = 1.6 \times 10^{22} \text{ cm}^{-2}$, an electron temperature of either ≈ 7 MK or 28 MK (corresponding to either of the higher temperatures found for T Tau N), and 6.1% of the total counts. We found $L_{X,0.3\text{--}10 \text{ keV}} = 4 \times 10^{30} \text{ erg s}^{-1}$ and $L_{X,0.3\text{--}10 \text{ keV}} = 1.4 \times 10^{30} \text{ erg s}^{-1}$, respectively, for the two temperatures. The true values may be higher if N_H is higher, but lower if we overestimated the count rate contributions in the marginal fit. In any case, given the small contribution compared to T Tau N and lack of strong significance, we will assume that the observed *XMM-Newton* spectra are from T Tau N.

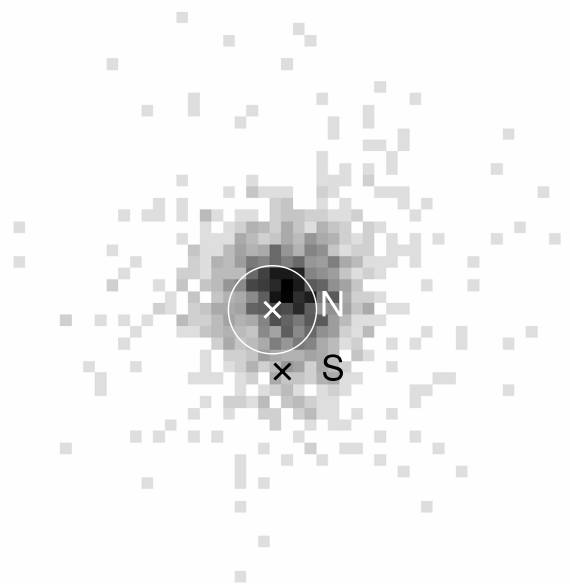


Fig. 1. The T Tau source on the *Chandra* HRC-I detector (pixel size: $0''.13$). The positions of T Tau N and S are marked by the crosses. The white circle around the expected T Tau N position indicates the 90% source location error for *Chandra*. There is a slight systematic offset of about $0''.27$ of the X-ray image relative to the true position of T Tau N ($-0''.11$ in RA, $+0''.25$ in declination in the sense “X-ray minus true”), which has not been corrected for in this figure.

5. The optical, UV, and X-ray light curves

Figure 2 shows the X-ray and ultraviolet light curves from the *XMM-Newton* observations.

We extracted the combined EPIC PN and MOS1 background-subtracted light curves for the softer and harder portion of the spectrum (energies of $0.4\text{--}1.0$ keV and $1.0\text{--}7.3$ keV, respectively; MOS2 was not used because of difficulties in defining a background curve in the small-window mode). These light curves are shown in the upper two panels of Fig. 2. Both count rates are slowly decaying, probably from a flare with a peak that appears to have been recorded at the beginning of the observation. The harder flux decays more rapidly but then also levels off earlier, leading to a hardness increase in the second half of the observation, illustrated in the third panel that shows the ratio “hard:soft”. The fourth panel shows the light curve for the entire spectral range. Note that during the first ≈ 1350 s, the PN camera did not record data (interval before the time marked by the left arrow). We scaled the MOS1 light curve by an average factor to the estimated PN+MOS1 count rate. Similarly, only the PN observed during the last 2830 s (time after the second arrow). The light curve has again been scaled from the PN count rate to the expected total count rate.

The OM UVW1 light curve is shown in the bottom panel. It was recorded in a series of exposures, each with a duration of ≈ 3540 s, followed by a gap of 340 s. A few exposures were not successfully recorded. The high count rate induced large coincidence losses which led to inaccurate calibration of the incident count rate in some exposures, visible as obvious discontinuities with respect to the count rates in previous or following exposures. The affected exposures were manually corrected by multiplying their count rates to produce a smoothly connected light curve (Fig. 2; the uncorrected fluxes are also shown; the count rates in the first exposure were not corrected and are uncertain given the long time gap before the second exposure).

³ The 90% source location error circle in *Chandra* has a radius of about $0.5''$, see *Chandra* Proposers’ Observatory Guide v.8.

⁴ <http://heasarc.gsfc.nasa.gov/Tools/w3pimms.html>

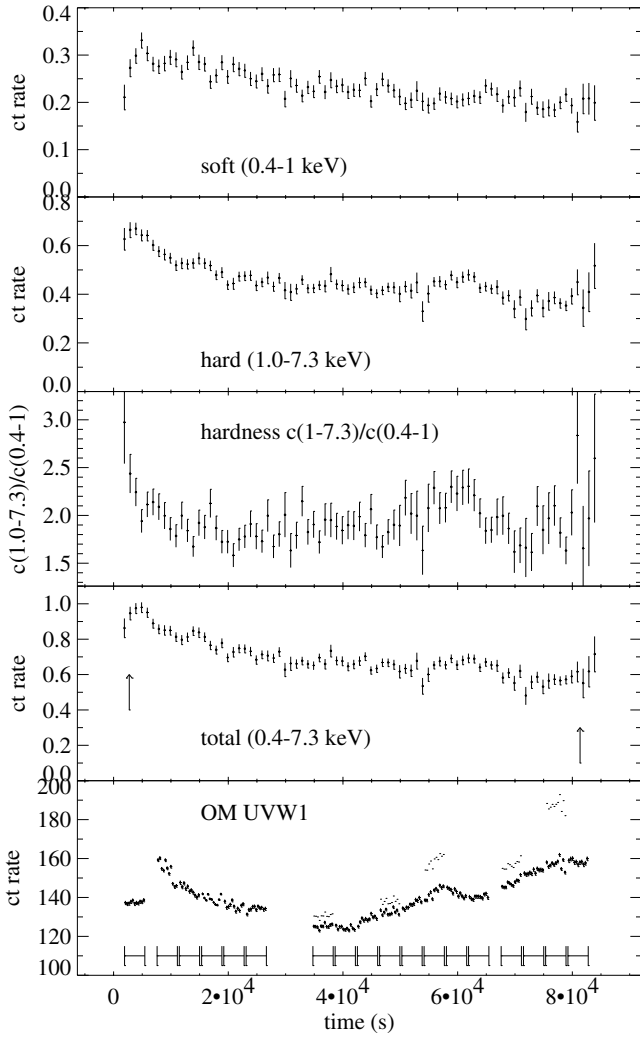


Fig. 2. Light curves of the T Tau source, extracted from the *XMM-Newton* observations. *From top to bottom*: combined EPIC PN+MOS1 light curve for soft (0.4–1 keV) counts; hard (1–7.3 keV) counts; hardness ratio, i.e., ratio between hard and soft count rates; total light curve (0.4–7.3 keV); the arrows mark the times between which both EPIC cameras were operational; and the OM UVW1 light curve (dots illustrate bin count rates before manual correction; see text for details). Horizontal bars give time intervals for each OM exposure.

Three features are to be mentioned: i) there is no detailed correlation between the X-ray and the UV light curves; ii) both curves show, however, a general decay in the first half of the observation, perhaps as a consequence of the weak flare seen in X-rays. The time of the UV peak is uncertain, given the unknown correction factor for the first exposure. It may have occurred before the start of the observations; iii) the UV light curve increases in the second half of the observation, in contrast to the X-rays. However, the X-ray hardness also increases, and both UV flux and hardness show a peak around $t = 6 \times 10^4$ s. It is possible that both features relate to a flare-like heating event that produced both hot coronal plasma (seen in the harder X-ray band) and enhanced emission in the chromosphere and transition region (seen in the UVW1 band).

The light curves in *UBVR* obtained at Mt. Maidanak Observatory during the ground-based monitoring period in 2003 around the observing campaign with *Chandra* are presented in Fig. 3. No overlap with the *Chandra* observing interval was achieved. These optical observations nearly cover the 2.8-day

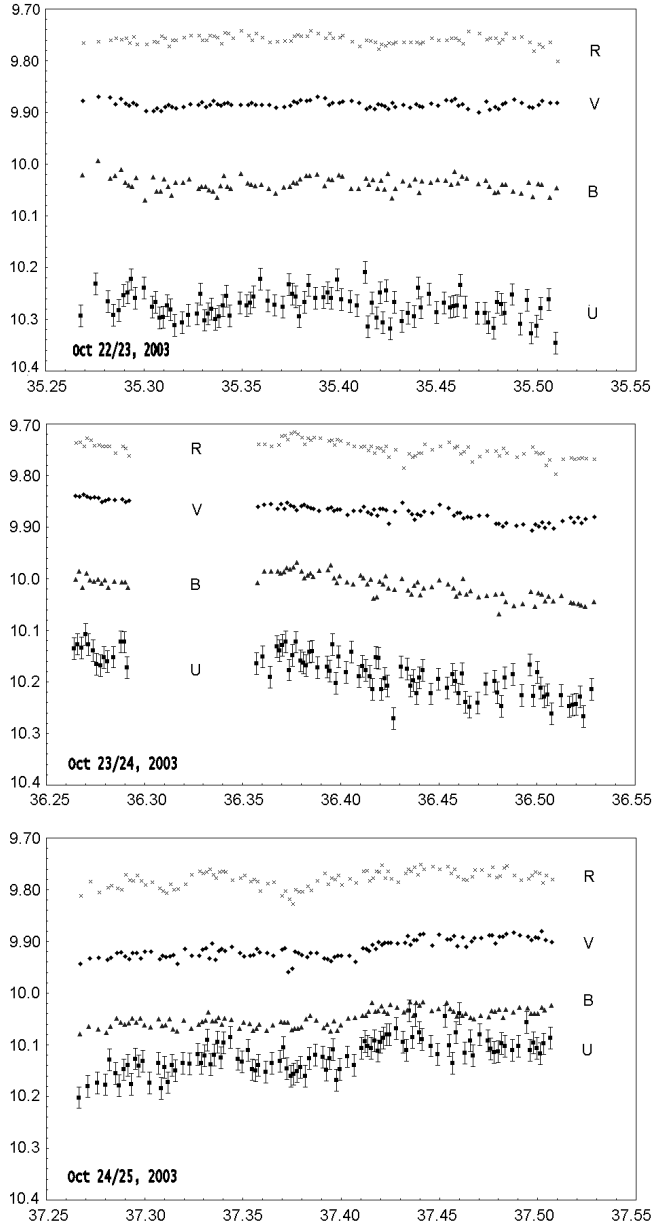


Fig. 3. Optical *UBVR* light curves of T Tau, collected during three consecutive nights (2003 October 22–25). The abscissae give JD-2452900.0, and the ordinates are in magnitudes. Both day-to-day variations and short-term fluctuations (in the *U* band) can be seen.

photometric period of T Tau (Herbst et al. 1986) which corresponds to the rotational period of the star. Our data show day-by-day variability of T Tau: while on October 22/23 the brightness of the star is rather stable, the brightness must have risen in all bands between the first and the second observation; prominent slopes can be seen in the light curves during the next two days, in opposite directions, first decreasing in brightness, then increasing again. Given that the rotation period of the star is 2.8 d, at least two minima and two maxima must have occurred during the stellar rotation covered by these observations. Magnetically active stars indeed often show two longitude intervals with preferred magnetic activity (e.g., Berdyugina et al. 1998). The amplitude of this variability seems to increase with decreasing wavelength and therefore reaches its maximum for the *U* band. This is particularly evident during the October 24/25 observation when the *U*-band curve approaches the *B*-band brightness.

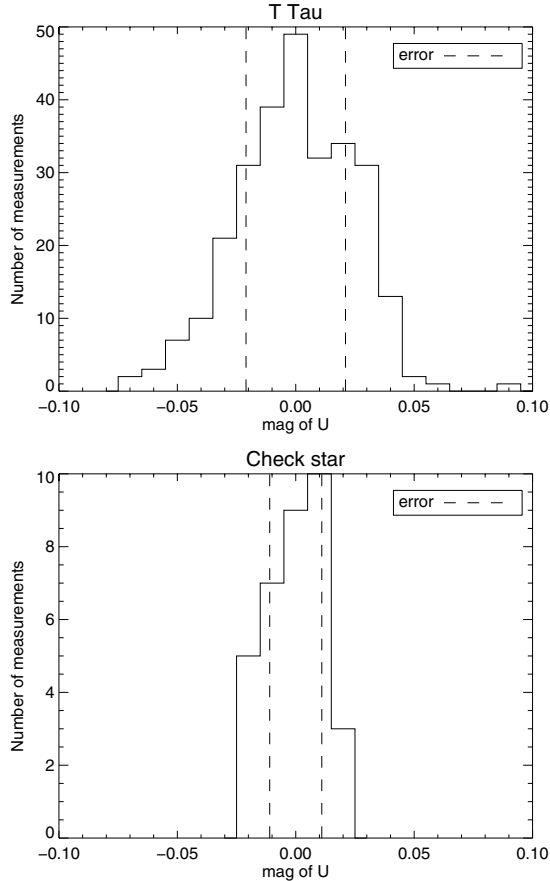


Fig. 4. Statistical analysis of variability in the U band light curve of T Tau (*top*) and the check star HD 284415 (*bottom*). The solid histograms give the number of measurements with a given magnitude offset from the average (after removing a slow trend for T Tau). The dashed lines mark the maximum rms error for a measurement at the average magnitude.

This day-by-day variability is similar to the long-term variations in the *XMM-Newton* UV light curve.

Another type of variability which is suggested in the U -band curve is defined by fast small-amplitude variations. In order to estimate the accuracy of our observations, we calculated histograms of the brightness distribution for both the check star and T Tau itself (Fig. 4). For the second and third T Tau observation, we first removed a slow trend in the brightness, using a polynomial fit that describes the nightly trend but no shorter features. The x -axis gives the deviation of points from the mean magnitude after removal of the trend. The maximum rms error of a single measurement in the U band calculated from the observations is 0.011 mag for the check star and 0.021 mag for T Tau (in the U band the check star was roughly three times brighter than T Tau). We plot these errors with dashed lines in the histograms. The histogram of T Tau suggests that some of the variability is due to real fluctuations beyond statistical errors, while this is not the case for the check star.

6. High-resolution X-ray spectroscopy

We present the combined and fluxed RGS1+2 spectrum in Fig. 5. Given the significant background radiation level, we prefer to first show the full spectrum before background subtraction and the background spectrum itself separately. The potential influence of background features on the spectrum at

the source position can thus be examined in detail. The unsubtracted spectrum also retains maximum signal-to-noise ratios to reveal weak line features. (We also inspected the spectrum extracted for low-background episodes only. Apart from a lower S/N, it very closely resembles the spectrum shown here.) For the subsequent quantitative spectral analysis, we will use background-subtracted RGS spectra and provide separate illustrations (see below). We mark all spectral line features that contained $\geq (3-4) \times 10^{-6}$ photons $\text{cm}^{-2} \text{s}^{-1}$, identifying the dominant ions contributing to the flux (a few of these lines may not be individually recognized in the spectrum). Dotted vertical lines point to the location of a few important fainter lines that remained undetected.

The spectrum is rich in lines, but also reveals a strong continuum shortward of 17 Å. The most unusual aspect of the T Tau X-ray spectrum is its mixture of features associated with extremely hot plasma, such as the continuum and several lines of highly-ionized Fe formed above 10 MK, and lines attributed to very cool plasma such as those from N VII and O VII. The ratio between the fluxes in the O VII He-like line triplet at 21.6–22.1 Å and the O VIII Ly α line at 18.97 Å is near unity. This is unusual for magnetically active main-sequence stars and WTTS, while other CTTS have shown similar ratios, as noted in a survey of TTS X-ray grating spectra presented by Telleschi et al. (2007b). Among main-sequence solar analogs, only inactive, old stars reveal such low flux ratios (Telleschi et al. 2005). We also note the unusually clear appearance of two He β lines of O VII, at 17.7 Å and at 18.6 Å and the presence of the Ly α line of N VII at 24.7 Å. On the other hand, several features in the unsubtracted spectrum coincident with the He α lines of N VI at 28.5–29.5 Å and the He β lines of N VI at 23.3 Å and at 23.8 Å are not significant because the background spectrum contains similar features at the respective wavelengths. We emphasize that the identified features of O VII do not suffer from irregular background.

We have performed spectral fits in XSPEC (Arnaud 1996), using the vpec collisional ionization equilibrium thermal line+continuum model combined with a common photoelectric absorption component, parameterized by the neutral hydrogen column density N_{H} . We use background-subtracted spectra for this analysis. The source spectrum is sufficiently rich in spectral features that a determination of several element abundances is warranted. We note that alternative methods such as reconstruction of emission measure distributions from extracted line fluxes could in principle be applied; however, most of the important line features required for such an analysis are heavily blended, and from no element (including Fe) do we see lines from more than two ionization stages at sufficient signal-to-noise ratios. We therefore prefer to use template spectra in XSPEC that take into account all unresolved blends and faint lines present in the code, while the principal thermal components are determined by the strongest lines and the continuum. A comparison between these two approaches for similar but brighter X-ray spectra from solar analogs has shown little difference (Telleschi et al. 2005).

We simultaneously fitted spectra of RGS1 and RGS2 between 7 Å and 25 Å, complemented with a portion of the MOS1 spectrum in the range of 1.5–9.35 Å. We use only one MOS spectrum confined to the harder range because we prefer to give full weight to the high-resolution RGS spectra wherever possible. The MOS spectrum complements information on the Mg, Si, S, and Fe abundances and constrains the hottest plasma components. All spectra were rebinned so that they contained at least 15 counts per bin before background subtraction. Three thermal components were required for a good

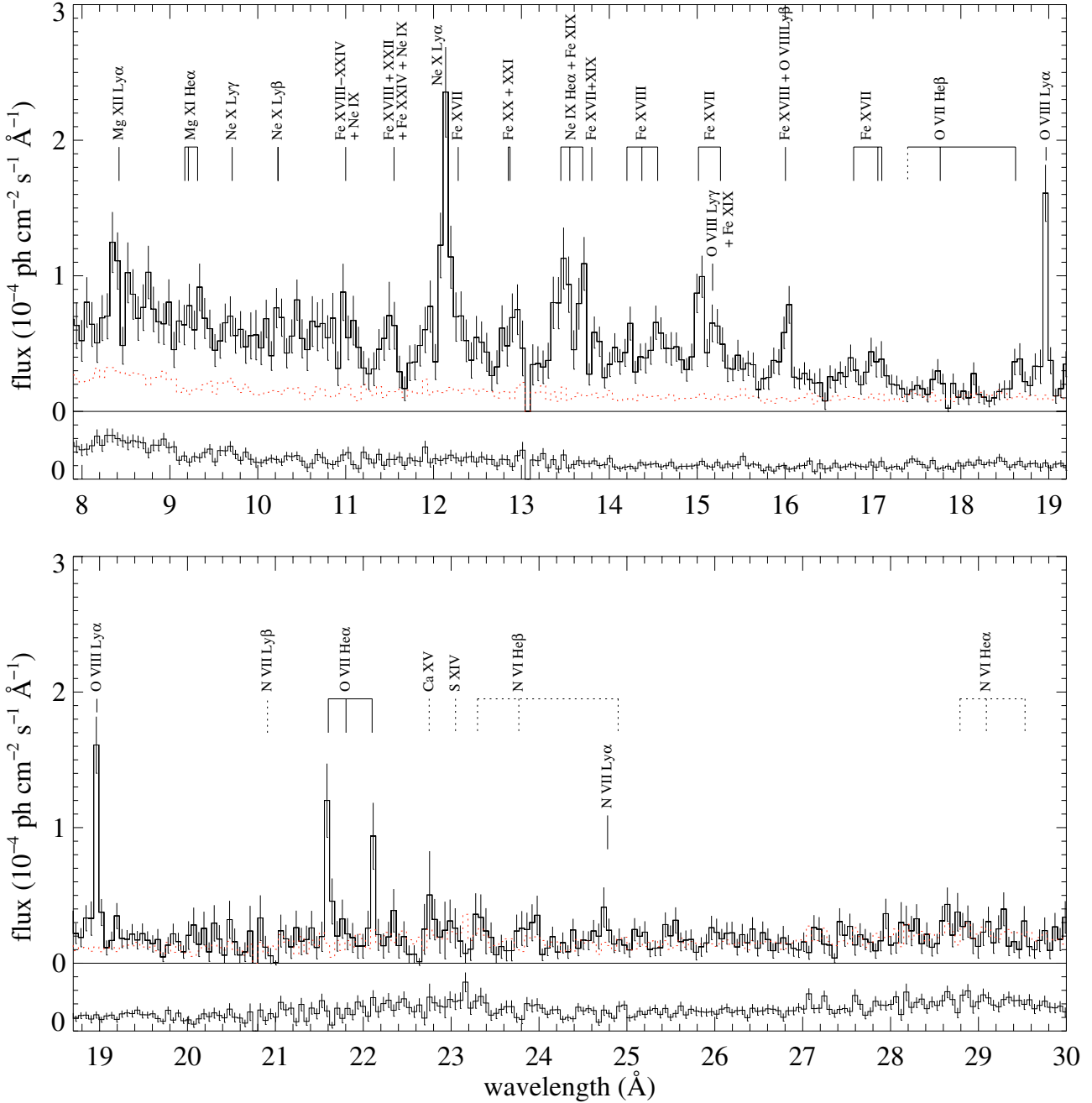


Fig. 5. Fluxed, combined RGS1+2 spectrum. The background has not been subtracted, but its spectrum is overplotted as a red, dotted histogram, and also separately shown in the narrow, lower panels on the same flux scale. The bin width is 58 mÅ. The brightest line features contributing to the model fit are labeled. A few important features that have not been detected are marked with dotted lines.

fit, defined by their temperatures $T_{1,2,3}$ and the associated emission measures $EM_{1,2,3}$. The results are shown in Table 2, together with 68% and 90% confidence ranges. The reduced χ^2 is excellent (1.09 for 382 degrees of freedom = d.o.f.). We also list the “average temperature” T_{av} , which has been defined as the logarithmic average of the three temperatures, weighted with the respective emission measures; its 68% range is an approximation calculated using Gaussian error propagation. This temperature is considerably lower than $T_{av} = 12.8\text{--}17.6$ MK found in the XEST survey from EPIC data (Güdel et al. 2007a). This is because the EPIC spectral fit does not recognize the softest emission for which the cool component at 1.8 MK is responsible. If we calculate T_{av} for the two hotter components, we obtain $T_{av} = 15.7$ MK, in agreement with the EPIC survey value.

The fits are illustrated in Fig. 6 for two spectral ranges of the RGS detectors. The RGS data are shown at a higher resolution (fewer counts per bin) than actually used for the fit, in order to better illustrate the individual line features.

The unusual mixture of very hot (≈ 30 MK) and very cool (≈ 1.8 MK) plasma is confirmed. In the intrinsic, unabsorbed model spectrum, the O VII resonance line is in fact *the strongest line in the entire X-ray spectrum*, exceeding even the O VIII Ly α line by a factor of 2.0. Such ratios are otherwise typical only for extremely inactive stars with cool coronae, such as Procyon (Raassen et al. 2002).

The amount of cool emission measure is similar to the total emission measure of the hotter two components although the precise ratio strongly depends on N_H ; the latter sensitively affects

Table 2. Results from the 3T model fit.

Parameter	Best-fit	68% range	90% range
N_{H} [10^{22} cm $^{-2}$]	0.49	0.46–0.55	0.43–0.59
T_1 [MK]	1.76	1.30–2.01	0.94–2.16
T_2 [MK]	7.42	7.11–7.69	6.91–7.87
T_3 [MK]	28.8	27.4–30.6	26.5–32.3
EM_1 [10^{53} cm $^{-3}$]	9.3	5.5–17.8	3.8–25.8
EM_2 [10^{53} cm $^{-3}$]	4.4	3.4–6.2	2.8–7.7
EM_3 [10^{53} cm $^{-3}$]	5.0	4.6–5.4	4.1–5.6
Abundances: ^a			
N	0.31	0.00–2.92	0.00–5.62
O	0.43	0.28–0.75	0.28–1.24
Ne	0.82	0.61–1.02	0.50–1.19
Mg	0.49	0.34–0.63	0.27–0.74
Si	0.27	0.17–0.37	0.12–0.44
S	0.30	0.17–0.44	0.09–0.54
Fe	0.28	0.21–0.35	0.18–0.40
T_{av} [MK]	5.2	4.2–7.3	...
n_e [10^{10} cm $^{-3}$]	...	<2.6	<8
$L_{\text{X},0.1-10}^b$ [10^{31} erg/s]	2.02
$L_{\text{X},0.3-10}^c$ [10^{31} erg/s]	1.52
χ_{red}^2	1.09
d.o.f.	382

^a Relative to solar photospheric abundances of Anders & Grevesse (1989) except for Fe, which refers to Grevesse & Sauval (1999); ^b for the 0.1–10 keV range, using a distance of 140 pc; ^c for the 0.3–10 keV range, using a distance of 140 pc.

the soft part of the spectrum to which the cool plasma mostly contributes. The value of $N_{\text{H}} \approx 4.9_{-0.3}^{+0.6} \times 10^{21}$ cm $^{-2}$ is somewhat higher than found from EPIC data alone (Güdel et al. 2007a), $N_{\text{H}} = (3.4 \pm 0.1) \times 10^{21}$ cm $^{-2}$ (from a 2-T analysis). Part of this discrepancy could be induced by slight, systematic calibration inaccuracies at the long-wavelength end of the RGS. Further, for spectra of limited S/N, an acceptable spectral fit could overestimate the cool EM if N_{H} is slightly too high. However, the basic result is evident in the flux ratios of the O VII and O VIII lines at similar wavelengths. We find a ratio between the observed fluxes in O VII and O VIII of 1.06 ± 0.29 . From the model, we infer that about half of the O VIII Ly α line flux is due to the two hotter components. The other half must be due to a cooler component and therefore amounts to about 50% of the total O VII flux at 21.6–22.1 Å. Keeping the hotter two components fixed in the model but enforcing $N_{\text{H}} = 3.4 \times 10^{21}$ cm $^{-2}$ as in the XEST survey (Güdel et al. 2007a, noting that N_{H} of this magnitude principally influences temperature and emission measure of the coolest component), we calculated conditions for T_1 and EM_1 to produce the observed flux ratio, given the contributions from the hotter components. There is a family of solutions for (T_1, EM_1) below $T_1 = 2.1$ MK, with the coolest emission measure still being 17% larger than EM_2 , and this solution is obtained for $T_1 = 1.59$ MK. We conclude that even for the lower N_{H} , the coolest emission measure is comparable to the intermediate and hotter EMs.

The element abundances (given with respect to solar photospheric abundances of Anders & Grevesse 1989, except for Fe for which we used the value of Grevesse & Sauval 1999 as a basis) are common among TTS (Telleschi et al. 2007b). We note a relatively large abundance ratio for Ne/Fe ($=2.9 \pm 1.0$). The abundance of N is very poorly determined, given the very low S/N of any potentially detected line. The usual trend toward an inverse first ionization effect in magnetically active

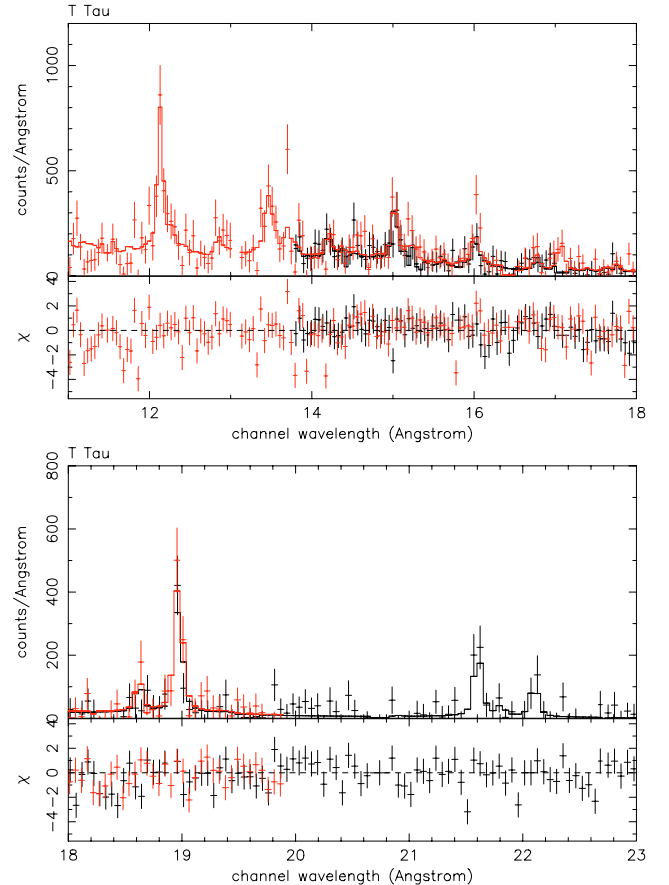


Fig. 6. Spectral fit to the background-subtracted RGS1 (black) and RGS2 (red) data in the 11–18 Å (top) and 18–23 Å (bottom) ranges. Note the missing data in the RGS1 spectrum below 13.8 Å and in the RGS2 spectrum above 20 Å. These gaps are due to chip failures earlier in the mission. The lower panels in each plot show the residuals in terms of sigmas.

stars (Brinkman et al. 2001; Güdel et al. 2001) is marginally recovered.

We used the O VII He-like line triplet at 21.6–22.1 Å to infer electron densities in the coolest plasma component. In high-density environments, the forbidden transition ($f, 1s2s\ ^3S_1 \rightarrow 1s^2\ ^1S_0$) at 22.1 Å can become suppressed by electron collisions in favor of the intercombination transitions ($i, 1s2p\ ^3P_{1,2} \rightarrow 1s^2\ ^1S_0$) at 21.8 Å (Gabriel & Jordan 1969; Blumenthal et al. 1972, see Telleschi et al. 2007b for applications to high-resolution spectra of other pre-main sequence stars). The density-sensitive range approximately covers 10^{10} cm $^{-3} \lesssim n_e \lesssim 10^{12}$ cm $^{-3}$. The limited S/N makes individual extraction of the three line fluxes difficult. The i line is not significantly detected, while the r and f lines are present (at the 2.3 and 3.6 σ level, respectively), suggesting low densities. Formally, the *unabsorbed* fluxes at the distance of the Earth are $(5.14 \pm 1.41, 0.91 \pm 0.95, 3.70 \pm 1.58) \times 10^{-4}$ photons cm $^{-2}$ s $^{-1}$ in the (r, i, f) lines, resulting in a best-fit f/i ratio of 4.0. However, we note that there is an additional constraint on the relative line fluxes. The so-called G ratio, $(r+i)/f$, where $r, i,$ and f denote the fluxes in the resonance, intercombination, and forbidden lines, is determined by the thermal structure of the plasma. We therefore fixed our best-fit thermal model and made use of the density calculations implemented in the vmekal code in XSPEC to infer the densities. We only fitted n_e and, for optimum adjustment of the line

fluxes, the emission measure of the coolest component that predominantly forms the lines. The high f/i ratio requires low densities. The best-fit values are below the density-sensitive range (in agreement with the above f/i estimate) so that we quote only the 68% and 90% upper limits in Table 2. These are approximately $2.6 \times 10^{10} \text{ cm}^{-3}$ (68% confidence) and $\approx 8 \times 10^{10} \text{ cm}^{-3}$ (90% confidence) using Gehrels weights on our spectral data⁵.

The X-ray luminosities, L_X , in Table 2 are given for the 0.3–10 keV range (adopted for the XEST survey, Güdel et al. 2007a) and also for the 0.1–10 keV range to include important contributions from the coolest component. The latter indeed doubles L_X compared to the EPIC analysis in Güdel et al. (2007a). Not considering the contributions from the cool plasma, we find $L_X = 1.0 \times 10^{31} \text{ erg s}^{-1}$ for the 0.3–10 keV range, nearly identical to the XEST survey value of $0.94 \times 10^{31} \text{ erg s}^{-1}$ based on a two-component spectral fit to the EPIC PN data.

7. Discussion and conclusions

7.1. Observational signatures

We now discuss the X-ray properties of T Tau N as found in this paper in the context of X-ray features that have previously been associated with accreting pre-main sequence stars, and with properties seen in the U -band and optical light curves. We address, in turn, the following characteristics: i) flux ratios in He-like triplets, indicative of electron densities; ii) cool plasma; iii) abundance anomalies; and iv) optical and ultraviolet variability. We refer to Telleschi et al. (2007b) and Telleschi et al. (2007c) for further detailed discussions of high-resolution X-ray spectra from pre-main sequence stars.

He-like line flux ratios and electron densities. High electron densities in cool plasma could be a consequence of accretion shocks. The post-shock temperature in the accretion column near the stellar surface is $T = 3v^2\mu m_p/16k$, where the velocity v is about 0.9 times the free-fall velocity $v_{\text{ff}} = (2GM/R)^{1/2}$ (Calvet & Gullbring 1998), m_p is the proton mass, k is the Boltzmann constant, and the mean molecular weight $\mu \approx 0.62$ for a fully ionized gas. For T Tau, we use $M = 2.4 M_\odot$ and $R = 3.6 R_\odot$ as listed in Güdel et al. (2007a). Then, $v_{\text{ff}} = 500 \text{ km s}^{-1}$ and $T \approx 2.9 \times 10^6 \text{ K}$. The soft excess is thus compatible with expected post-shock temperatures of the free-falling gas.

The accretion rate of T Tau is $\dot{M}_{\text{acc}} \approx (3\text{--}6) \times 10^{-8} M_\odot \text{ yr}^{-1}$ (White & Ghez 2001; Calvet et al. 2004). For the accretion luminosity, we use the expression given by Telleschi et al. (2007c) but for a somewhat larger corotation radius: $L_{\text{acc},30} \approx 820 \dot{M} \dot{M}_{-8} / \dot{R}$, where $L_{\text{acc},30} = L_{\text{acc}} / (10^{30} \text{ erg s}^{-1})$, $\dot{M} = M / M_\odot$, $\dot{M}_{\text{acc},-8} = \dot{M}_{\text{acc}} / 10^{-8} M_\odot \text{ yr}^{-1}$ and $\dot{R} = R / R_\odot$. We thus obtain $L_{\text{acc},30} = 1600\text{--}3200$, i.e., at least two orders of magnitude more than required to produce the radiative output in the softest X-rays. Some energy will be conducted to cooler layers, and the majority of the X-rays may be entirely absorbed (Lamzin 1999).

Lastly, we can estimate the shock density, using the strong-shock condition $n_2 = 4n_1$, where n_1 and n_2 are the pre-shock and post-shock densities, the former relating to the mass accretion rate and the accreting surface fraction F (filling factor –

assuming that all flows produce similar shocks). Telleschi et al. (2007b) gave the expression

$$n_2 \approx \frac{4 \times 10^{11} \dot{M}_{-8}}{\dot{R}^{3/2} \dot{M}^{1/2} F} [\text{cm}^{-3}]. \quad (1)$$

Typical values for F are $F = 0.1\text{--}10\%$ (Calvet & Gullbring 1998). For T Tau, the density should then be $n_2 = (3.6\text{--}7.2) \times 10^9 \dot{M}_{-8} / F \text{ cm}^{-3} = (1.1\text{--}2.2) \times 10^{11} / F \text{ cm}^{-3} \gtrsim 1.1 \times 10^{12} \text{ cm}^{-3}$, where the latter value is for the extreme case of $F = 10\%$, while we obtain $n_e \approx (1.1\text{--}2.2) \times 10^{14} \text{ cm}^{-3}$ for $F = 0.1\%$. Calvet et al. (2004) derived a filling factor of $F = 3.1\%$ specifically for T Tau. This implies $n_e \approx (3.5\text{--}7.1) \times 10^{12} \text{ cm}^{-3}$. These values are orders of magnitude larger than the densities (or upper limits thereof) inferred from the O VII triplet. In contrast, the T Tau density upper limit ($\approx 8 \times 10^{10} \text{ cm}^{-3}$ at the 90% confidence level) is fully compatible with the measured densities of (mostly magnetically active) main-sequence coronae reported by Ness et al. (2004). These are distributed between $< 10^{10} \text{ cm}^{-3}$ and about 10^{11} cm^{-3} (derived from O VII), the median and mean $\log n_e$ values being 10.36 and 10.37 ± 0.06 , respectively (as derived from the Kaplan-Meier estimator analysis in ASURV which also takes upper limits into account; Feigelson & Nelson 1985; LaValley et al. 1992).

We also inspected the Ne IX density-sensitive triplet formed at somewhat higher temperatures ($\approx 4 \text{ MK}$). The signal-to-noise ratio is low and the Ne IX triplet is strongly blended with several lines of highly ionized Fe. Nevertheless, there is a clear indication of a strong f line in that triplet as well, again pointing to low densities (the Ne triplet is density-sensitive in the range of approximately $n_e \approx 10^{11}\text{--}10^{13} \text{ cm}^{-3}$).

In summary, then, standard accretion shock physics does not seem to be compatible with a shock-heating scenario for the soft spectral component forming the bulk of the O VII (and Ne IX) lines in T Tau. We emphasize that T Tau is now the second accreting pre-main sequence star that shows a high f/i flux ratio, after similar reports on the Herbig star AB Aur (Telleschi et al. 2007c). This is to be compared with three CTTS previously reported to show high densities, $n_e > 10^{11} \text{ cm}^{-3}$, namely TW Hya (Kastner et al. 2002), BP Tau (Schmitt et al. 2005), and V4046 Sgr (Günther et al. 2006).

Abundance anomalies. High abundances of the volatile elements N and Ne in TW Hya with respect to the Fe abundance have been suggested to be due to stronger condensation of Fe and some other elements to dust grains in the circumstellar disk (Stelzer & Schmitt 2004). If the star preferentially accretes from the gas phase, then an elevated Ne/Fe ratio would be measured in the coronal or shock-heated plasma.

Anomalously high Ne abundances have been found in the X-ray source of TW Hya (Kastner et al. 2002; Stelzer & Schmitt 2004), but also in non-accreting evolved stars such as members of the RS CVn class (Ne/Fe abundance ratios up to 13.4, Audard et al. 2003), and in pre-main sequence stars thought to be non-accreting (weak-line) TTS, such as TWA 5 (Ne/Fe ≈ 10 ; Argiroffi et al. 2005) and HD 98800 (Ne/Fe ≈ 5 ; Kastner et al. 2004b). Telleschi et al. (2007b) have systematically analyzed RGS spectra of pre-main sequence stars and compared Fe/Ne and Fe/O abundance ratios for them. They found that i) both ratios tend to be higher for young G-type stars than for K- or M-type stars; this trend still holds for near-zero-age main-sequence stars; and ii) there is no difference between CTTS and WTTS with regard to this trend.

Figure 7 shows the Fe/Ne ratio derived from high-resolution spectroscopy as a function of spectral type for TTS and ZAMS stars (for references, see Telleschi et al. 2007b).

⁵ We confirmed these estimates using Monte Carlo simulations based on the observed source spectrum, the observed background spectrum, the same response matrix and exposure time, and the thermal structure and abundances as found in our best fit to the entire spectrum; we obtained a 68% limit at $2 \times 10^{10} \text{ cm}^{-3}$ and a 90% limit around $\approx 9 \times 10^{10} \text{ cm}^{-3}$. Conversely, if the true density were 10^{11} cm^{-3} , we found that only one out of ten statistical realizations converges to an inferred density below $\approx 2 \times 10^{10} \text{ cm}^{-3}$.

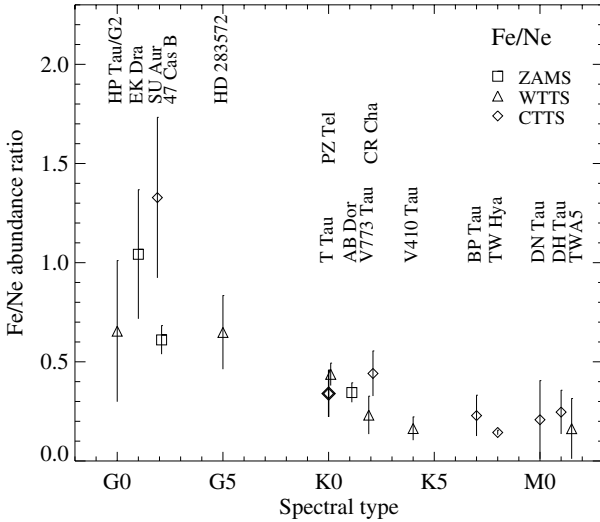


Fig. 7. The Fe/Ne abundance ratio in the X-ray sources of various pre-main sequence stars and ZAMS stars as a function of spectral class. The abundance measurements for stars other than T Tau were taken from the previous literature and from Telleschi et al. (2007b) (see that paper for a comprehensive description and references; values were converted, if necessary, to refer to the solar photospheric abundances of Anders & Grevesse 1989 and, for Fe, Grevesse & Sauval 1999). The value determined in the present work for T Tau is shown in bold face. Symbols mark different types of stars: squares: ZAMS stars; triangles: WTTS; diamonds: CTTS.

The trend for an increasing ratio toward earlier spectral types is clearly seen, independently of the evolutionary status (CTTS, WTTS, ZAMS). The ratio for T Tau fits in well for a K0 star. The same holds true for the Fe/O ratio (not shown; see Telleschi et al. 2007b). We conclude that the abundances observed in T Tau follow a trend that holds for a larger sample of young stars, and this trend – as judged from a still small sample of stars – does not seem to be related to accretion properties.

Soft excess. The most outstanding property of the old CTTS TW Hya is its extremely soft X-ray emission (Kastner et al. 2002; Stelzer & Schmitt 2004). However, no such X-ray sources have been identified in large samples of CTTS in Orion (Preibisch et al. 2005) or in Taurus (Güdel et al. 2007a). On the other hand, Telleschi et al. (2007b) have suggested that, apart from a dominant hot plasma, there is a *soft excess* in accreting pre-main sequence stars, best revealed by an unusually large ratio between the (summed) photon fluxes in the O VII He-like triplet and the O VIII Ly α line, found to be around unity for CTTS but typically less than 0.5 for WTTS. The intrinsic ratio between the luminosities of these lines is of course altered by photoelectric absorption, i.e., the O VII/O VIII ratio tends to decrease for increasing N_{H} . The N_{H} value for T Tau compares with the largest in the Telleschi et al. (2007b) sample, yet the observed flux ratio is also among the largest. As reported above, we found a ratio of 1.06 ± 0.29 . In the unabsorbed model spectrum, the O VII r line is even a factor of two stronger than the O VIII Ly α line, and in fact is the strongest line in the X-ray spectrum.

T Tau thus confirms the conjecture that CTTS reveal a soft excess, despite the dominance of an extremely hard component in the overall X-ray spectrum. T Tau is the most extreme case for a soft excess in any TTS studied by high-resolution spectroscopy, except for TW Hya in which the soft component entirely dominates.

Optical and ultraviolet variability. Accretion shocks induce excess emission at short optical and ultraviolet wavelengths. Variability in these bands seen in accreting TTS has therefore been attributed to short-term variations in the mass accretion, or simply inhomogeneities at certain locations in the streams, rather than to flare-like energy release events (Gullbring et al. 1996). Variability amplitudes are typically modest (a few tenths of a magnitude) and last for 0.6 h to several hours. The gas heats only moderately, again in contrast to chromospheric gas in flares (Gullbring et al. 1996). The induced variability may be explained by accretion rate changes of the order of 10%, which will then require a scale length of the inhomogeneities of 5×10^{10} cm for the CTTS BP Tau and, combined with the free fall velocity, correctly explains the variability time scales (see Gullbring et al. 1996, for further details). It is possible that these inhomogeneities reflect in variations of the softest X-ray flux if X-rays are produced in the accretion shock, but a dedicated monitoring study of BP Tau with ROSAT and ground-based *UBVRI* photometry revealed an absence of correlated events; X-ray variability may thus not be related to accretion-induced optical and UV variability (Gullbring et al. 1997). New evidence was provided by the comprehensive XEST survey: a comparison of the X-ray light curves of many TTS with simultaneous light curves obtained in the *U* band or a shorter-wavelength ultraviolet band showed little correlated behavior, except for a few examples of flares that were observed in both bands (Audard et al. 2007).

There is mixed evidence in our data. First, both the *XMM-Newton* ultraviolet data and the ground-based *U*-band data show clear evidence for both day-to-day variations and short-term variability. The former shows time scales of at least half a day, compatible with modulation of accretion hot spots due to rotation. The short-term events (e.g., at 6×10^4 s in Fig. 2, or at 37.35 d in the bottom panel of Fig. 3) are similar to those reported by Gullbring et al. (1996). Conclusions are ambiguous, however: During the *XMM-Newton* observations, there is a long-term trend in X-ray *hardness* that appears to correlate with the UV flux; in particular, there is a decay from the beginning of the observation that may be related to flare emission. The harder X-rays seen in our spectra cannot be produced by accretion shocks as the infall velocity is too low (see above). Some of the variations of the UV flux may therefore be due to an excess in chromospheric and transition region heating (producing excess UV emission) in concert with coronal heating (producing harder X-rays). Also, the short event at 6×10^4 s in the UV appears to be reflected in the X-ray hardness curve. The temporal relation is typical for flares: The ultraviolet excess, a signature of impulsive heating of the chromosphere, precedes the X-ray signal, a consequence of filling of magnetic loops with hot plasma. Thus, overall a significant contribution to UV variability may come from coronal energy release events, although a clear distinction is difficult. This view is supported by the large survey presented by Audard et al. (2007) that shows several obvious X-ray flares with correlated *U*-band or ultraviolet features.

Modulation effects due to rotation are also possible. The *UBVR* observations in Fig. 3 show some evidence (e.g., within the middle or the lower panels, or between the upper and middle panels) for a correlation between *B* or *V* magnitude and the *U*-*B* color, indicating that the source is bluer when brighter and redder when fainter. This is expected for both heated regions and cool spots. Heated regions could be due to either accretion hot spots or magnetically active chromospheric regions. However, the inclination angle of T Tau is small, $i = 19$ – 23 deg (Herbst et al. 1997; Eisloffel & Mundt 1998). Rotationally modulated surface features must therefore be located at latitudes of

approximately ± 20 deg around the equator. The standard magnetic accretion scenario (e.g., Calvet & Gullbring 1998) predicts that accretion hot spots form at high latitudes. It is therefore more likely that, at least during our *UBVR* observations, the modulation was due to active regions (unless the accretion also occurs along more complicated magnetic field structures toward equatorial regions). The indication of (at least) two minima and two maxima in Fig. 3 could be due to two preferred active longitudes producing chromospherically active regions near the equator (e.g., Berdyugina et al. 1998).

7.2. Implications for models

Our discussion thus points to the following conclusions: i) if mass accretion streams induce X-rays in shocks near the surface, then densities should be much higher than inferred from the observed density-sensitive line flux ratios. It is possible that some of the observed X-ray emission originates in accretion shocks, but only a fraction of the accretion stream, subject to very low densities, would be responsible; ii) abundance anomalies do not seem to reflect accretion properties, and T Tau is no exception; iii) T Tau is, however, the most outstanding example, apart from TW Hya, of an accreting TTS with a soft excess in the X-ray spectrum. Such excess is not found in non-accreting young stars. We thus suggest that the X-ray production of T Tau is influenced by the accretion process although the X-rays may not form in the bulk of the accretion footpoints.

Shocks could form in outflows and jets that are related to the accretion process (see Güdel et al. 2005, for the example of DG Tau A). In that case, low temperatures and low densities would be expected. Since T Tau does drive outflows and is surrounded by Herbig-Haro objects (see references in Sect. 1), this possibility cannot be excluded, but explicit evidence is lacking. The high-resolution *Chandra* HRC image (Fig. 1) does not show any evidence for emission that might be related to a jet, in contrast to what has been found for DG Tau A (Güdel et al. 2005). The entire X-ray spectrum can be explained by a multi-thermal plasma subject to an overall photoelectric absorption component, again in contrast to the spectra of proposed jet-related X-ray sources (Güdel et al. 2007b).

An alternative location for the interaction between the plasma heating process and accretion is the corona or magnetosphere itself. Accreting material is guided along magnetic field lines and can increase the density in these regions considerably (similar to the estimates presented for the footpoints of the accretion flows, see above). Depending on the stream density and the strength of the magnetic fields near the accretion streams, the magnetic geometry may be considerably shaped by the mass stream itself; magnetic field lines be straightened by the flow, perhaps suppressing coronal magnetic energy release so that coronal heating may have little or no effect on infalling gas.

If, however, a small fraction of the mass loads onto magnetic fields of active coronal regions, it will lower the overall temperature and slightly increase the density there; cooling thus also becomes more efficient. A fraction of the coronal volume affected by a small amount of the infalling material could thus produce a cool coronal component, i.e., an observable soft excess. A suggestion along those lines was made by Preibisch et al. (2005) who proposed that the lower L_X/L_{bol} ratio of CTTS compared to WTTS in Orion is due to accretion flows completely suppressing coronal heating in the respective magnetospheric regions.

We estimate what fraction of the accreting material would have to be heated to $T = 1.8$ MK as observed in the softest component, assuming that the entire soft component is emitted by

such material (rather than by plasma evaporating from the stellar surface). We provide this estimate for the limiting case that any parcel of inflowing material that becomes subject to coronal heating is heated to T at once, after which it is permanently cooling by radiation, without further heating. The energy rate to heat accreting, ionized gas to $T = 1.8$ MK is $\dot{E} \approx 3kTN_e$ for hydrogen gas, where \dot{N}_e is the rate of new, cool electrons flowing into the heating region; there is an equal rate of protons. Adopting $\dot{M}_{\text{acc}} \approx (3-6) \times 10^{-8} M_{\odot} \text{ yr}^{-1}$ for the total accretion rate, we find $\dot{N}_e = (1.1-2.2) \times 10^{42} z \text{ s}^{-1}$, where z is the fraction of the infalling gas stream that is heated. Therefore $\dot{E} \approx (8-16) \times 10^{32} z \text{ erg s}^{-1}$. We assume that all energy is radiatively lost by the plasma at 1.8 MK. Modeling the energy losses of the cool plasma component in XSPEC, we find that only 17% of the radiative power is emitted above 0.3 keV, or 28% above 0.1 keV. Because the cool component emits $5.2 \times 10^{30} \text{ erg s}^{-1}$ into the 0.3–10 keV band (Sect. 6), the total radiative energy loss rate of this plasma is $3 \times 10^{31} \text{ erg s}^{-1}$. We conclude that $z = 1.9-3.8\%$ of the accretion flow would need to be heated to low coronal temperatures. This fraction will be smaller if the gas is continually heated while radiating.

We conclude, then, that T Tau implies an important role of accretion in the production of high-energy emission. We suggest that part of the accreting material adds a cool coronal component by being heated to modest temperatures while flowing into active regions. We are not able to predict why the X-ray excess is found at temperatures of about 2 MK, but we suggest that the additional loading of magnetic fields by cool, accreting mass will suppress heating to the otherwise common coronal temperatures of > 10 MK.

Acknowledgements. We thank Svetlana Berdyugina for helpful comments on photometry and active longitudes. We warmly acknowledge financial support by the International Space Science Institute (ISSI) in Bern to the *XMM-Newton* XEST team. X-ray astronomy research at PSI has been supported by the Swiss National Science Foundation (grants 20-66875.01 and 20-109255/1). Part of this research is based on observations obtained with *XMM-Newton*, an ESA science mission with instruments and contributions directly funded by ESA member states and the USA (NASA). M.A. acknowledges support by NASA grants NNG05GQ13G and NNG05GF92G for the *XMM-Newton* project. In addition, he acknowledges support from a Swiss National Science Foundation Professorship (PP002-110504). Support for this work was provided by the National Aeronautics and Space Administration through *Chandra* Award Number SAO GO3-4004X issued by the *Chandra* X-Ray Observatory Center, which is operated by the Smithsonian Astrophysical Observatory for and on behalf of the National Aeronautics and Space Administration under contract NAS8-03060.

References

- Anders, E., & Grevesse, N. 1989, *Geochim. Cosmochim. Acta*, 53, 197
- Akeson, R. L., Koerner, D. W., & Jensen, E. L. N. 1998, *ApJ*, 505, 358
- Argiroffi, C., Maggio, A., Peres, G., Stelzer, B., & Neuhauser, R. 2005, *A&A*, 439, 1149
- Arnaud, K. A. 1996, in *Astronomical Data Analysis Software and Systems V*, ed. G. Jacoby, & J. Barnes (San Francisco: ASP), ASP Conf. Ser., 101, 17
- Audard, M., Güdel, M., Sres, A., Raassen, A. J. J., & Mewe, R. 2003, 398, 1137
- Audard, M., Güdel, M., Skinner, S. L., et al. 2005, *ApJ*, 635, L81
- Audard, M., Briggs, K. R., Grosso, N., et al. 2007, *A&A*, 468, 379
- Berdyugina, S. V., & Tuominen, I. 1998, *A&A*, 336, L25
- Blumenthal, G. R., Drake, G. W. F., & Tucker, W. H. 1972, *ApJ*, 172, 205
- Bouvier, J., Cabrit, S., Fernández, M., Martín, E. L., & Matthews, J. M. 1993, *A&A*, 272, 176
- Brinkman, A. C., Behar, E., Güdel, M., et al. 2001, *A&A*, 365, L162
- Calvet, N., & Gullbring, E. 1998, *ApJ*, 509, 802
- Calvet, N., Muzerolle, J., Briceño, C., et al. 2004, *AJ*, 128, 1294
- den Herder, J. W., Brinkman, A. C., Kahn, S. M., et al. 2001, *A&A*, 365, L7
- Drake, J. J. 2005, in *Cool Stars, Stellar Systems and the Sun 13*, ed. F. Favata et al., ESA SP-560, 519
- Duchêne, G., Ghez, A. M., & McCabe, C. 2002, *ApJ*, 568, 771
- Duchêne, G., Ghez, A. M., McCabe, C., & Ceccarelli, C. 2005, *ApJ*, 628, 832

- Duchêne, G., Beust, H., Adjali, F., Konopacky, Q. M., & Ghez, A. M. 2006, *A&A*, 457, L9
- Dyck, H. M., Simon, T., & Zuckerman, B. 1982, *ApJ*, 255, L103
- Eislöffel, J., & Mundt, R. 1998, *AJ*, 115, 1554
- Feigelson, E. D., & DeCampli, W. M. 1981, *ApJ*, 243, L89
- Feigelson, E. D., & Nelson, P. I. 1985, *ApJ*, 293, 192
- Feigelson, E. D., & Montmerle, T. 1999, *ARA&A*, 37, 363
- Feigelson, E. D., Townsley, L., Güdel, M., & Stassun, K. 2007, *Protostars and Planets V*, ed. B. Reipurth, D. Jewitt, & K. Keil (Tucson: University of Arizona Press), 313
- Flaccomio, E., Micela, G., Sciortino, S., et al. 2005, *ApJS*, 160, 450
- Freeman, P. E., Doe, S., & Siemiginowska, A. 2001, *SPIE*, 4477, 76
- Gabriel, A. H., & Jordan, C. 1969, *MNRAS*, 145, 241
- Grevesse, N., & Sauval, A. J. 1999, *A&A*, 347, 348
- Grosso, N., Briggs, K. R., Güdel, M., et al. 2007, *A&A*, 468, 391
- Güdel, M. 2002, *ARA&A*, 40, 217
- Güdel, M. 2004, *A&ARv*, 12, 71
- Güdel, M., Audard, M., Briggs, K., et al. 2001, *A&A*, 365, L336
- Güdel, M., Skinner, S. L., Briggs, K. R., et al. 2005, *ApJ*, 626, L53
- Güdel, M., Briggs, K. R., Arzner, K., et al. 2007a, *A&A*, 468, 353
- Güdel, M., Telleschi, A., Audard, M., et al. 2007b, *A&A*, 468, 515
- Günther, H. M., Liefke, C., Schmitt, J. H. M. M., Robrade, J., & Ness, J.-U. 2006, *A&A*, 459, L29
- Gullbring, E., Barwig, H., Chen, P. S., Gahm, G. F., & Bao, M. X. 1996, *A&A*, 307, 791
- Gullbring, E., Barwig, H., & Schmitt, J. H. M. M. 1997, *A&A*, 324, 155
- Herbst, W., Booth, J. F., Chugainov, P. F., et al. 1986, *ApJ*, 310, L71
- Herbst, T. M., Robberto, M., & Beckwith, S. V. W. 1997, *AJ*, 114, 744
- Imanishi, K., Koyama, K., & Tsuboi, Y. 2001, *ApJ*, 557, 747
- Jansen, F., Lumb, D., Altieri, B., et al. 2001, *A&A*, 365, L1
- Kastner, J. H., Huenemoerder, D. P., Schulz, N. S., Canizares, C. R., & Weintraub, D. A. 2002, *ApJ*, 567, 434
- Kastner, J. H., Richmond, M., Grosso, N., et al. 2004a, *Nature*, 430, 429
- Kastner, J. H., Huenemoerder, D. P., Schulz, N. S., et al. 2004b, *ApJ*, 605, L49
- Kastner, J. H., Richmond, M., Grosso, N., et al. 2006, *ApJ*, 648, L43
- Koresko, C. D. 2000, 531, L147
- Koyama, K., Maeda, Y., Ozaki, M., et al. 1994, *PASJ*, 46, L125
- Lamzin, S. A. 1999, *Astron. Lett.*, 25, 430
- LaValley, M., Isobe, T., & Feigelson, E. 1992, in *Astronomical Data Analysis Software and Systems I*, ed. D. M. Worrall, C. Biemesderfer, & J. Barnes (San Francisco: ASP), 245
- Loinard, L., Mioduszewski, A. J., Rodríguez, L. F., et al. 2005, *ApJ*, 619, L179
- Mason, K. O., Breeveld, A., Much, R., et al. 2001, *A&A*, 365, L36
- Mel'nikov, S. Yu., & Grankin, K. N. 2005, *Astron. Lett.*, 31, 109
- Momose, M., Ohashi, N., Kawabe, R., Hayashi, M., & Nakano, T. 1996, *ApJ*, 470, 1001
- Murray, S. S., Austin, G. K., Chappell, J. H., et al. 2000, *SPIE*, 4012, 68
- Ness, J.-U., & Schmitt, J. H. M. M. 2005, *A&A*, 444, L41
- Ness, J.-U., Güdel, M., Schmitt, J. H. M. M., Audard, M., & Telleschi, A. 2004, *A&A*, 427, 667
- Neuhäuser, R., Sterzik, M. F., Schmitt, J. H. M. M., Wichmann, R., & Krautter, J. 1995, *A&A*, 297, 391
- Phillips, R. B., Lonsdale, C. J., & Feigelson, E. D. 1993, *ApJ*, 403, L43
- Preibisch, T., Kim, Y.-C., Favata, F., et al. 2005, *ApJS*, 160, 401
- Robrade, J., & Schmitt, J. H. M. M. 2006, *A&A*, 449, 737
- Raassen, A. J. J., Mewe, R., Audard, M., et al. 2002, *A&A*, 389, 228
- Schmitt, J. H. M. M., Robrade, J., Ness, J.-U., Favata, F., & Stelzer, B. 2005, *A&A*, 432, L35
- Skinner, S. L., & Brown, A. 1994, *ApJ*, 107, 1461
- Skinner, S. L., Gagné, M., & Belzer, E. 2003, *ApJ*, 598, 375
- Smith, K., Pestalozzi, M., Güdel, M., Conway, J., & Benz, A. O. 2003, *A&A*, 406, 957
- Solf, J., & Böhm, K.-H. 1999, *ApJ*, 523, 709
- Stelzer, B., & Schmitt, J. H. M. M. 2004, *A&A*, 418, 687
- Stelzer, B., Neuhäuser, R., & Hambaryan, V. 2000, *A&A*, 356, 949
- Strüder, L., Briel, U., Dennerl, K., et al. 2001, *A&A*, 365, L18
- Telleschi, A., Güdel, M., Briggs, K., et al. 2005, *ApJ*, 622, 653
- Telleschi, A., Güdel, M., Briggs, K. R., Audard, M., & Palla, F., 2007a, *A&A*, 468, 425
- Telleschi, A., Güdel, M., Briggs, K. R., Audard, M., & Scelsi, L. 2007b, *A&A*, 468, 443
- Telleschi, A., Güdel, M., Briggs, K. R., et al. 2007c, *A&A*, 468, 541
- Tsujimoto, M., Koyama, K., Tsuboi, Y., Goto, M., & Kobayashi, N. 2002, *ApJ*, 566, 974
- Turner, M. J. L., Abbey, A., Arnaud, M., et al. 2001, *A&A*, 365, L27
- van Langevelde, H. J., van Dishoeck, E. F., & Blake, G. A. 1994a, *ApJ*, 425, L45
- van Langevelde, H. J., van Dishoeck, E. F., van der Werf, P. P., & Blake, G. A. 1994b, *A&A*, 287, L25
- Vuong, M. H., Montmerle, T., Grosso, N., et al. 2003, *A&A*, 408, 581
- Walter, F. M. 1986, *ApJ*, 306, 573
- Walter, F. M., & Kuhl, L. V. 1981, *ApJ*, 250, 254
- Weisskopf, M. C., Brinkman, B., Canizares, C., et al. 2001, *PASP*, 114, 1
- White, R. J., & Ghez, A. M. 2001, *ApJ*, 556, 265
- Wolk, S. J., Harnden, F. R. Jr., Flaccomio, E., et al. 2005, *ApJS*, 160, 423